Supplementary Information

Spatiotemporal photon distribution control on active sites enables bio-inspired methane-to-methanol conversion

Yi Li[1,2], Yuehan Cao*[1,2], Chunqiu Han[2], Kaibo Zheng[3], Shaowen Cao[4], Jie Meng[5] & Ying Zhou*[1,2]

[1]State Key Laboratory of Oil and Gas Reservoir Geology and Exploitation, Southwest Petroleum University, Chengdu 610500, China

[2]School of New Energy and Materials, Southwest Petroleum University, Chengdu 610500, China

[3]Department of Chemical Physics and NanoLund Chemical Center, Lund University P.O. Box 124, 22100 Lund, Sweden

[4]State Key Laboratory of Advanced Technology for Materials Synthesis and Processing, Wuhan University of Technology, Wuhan, 430070, China

[5]Department of Chemistry, Technical University of Denmark, DK-2800 Kongens Lyngby, Copenhagen 2800, Denmark

*Correspondence and requests for materials should be addressed to Y.C. (e-mail: yhcao419@163.com) and Y.Z. (email: yzhou@swpu.edu.cn).

Table of Contents

Supplementary Figures

1. Preparation of photocatalysts and XRD

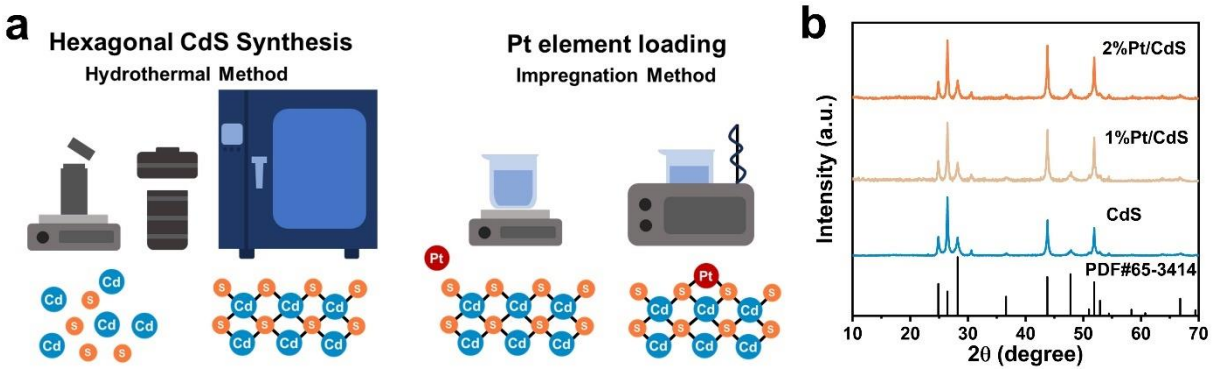

Supplementary Fig. 1 Preparation of photocatalysts and XRD. a Schematic diagram (created using Microsoft Powerpoint software) illustrating the synthetic process and **b** XRD of CdS, 1%Pt/CdS and 2%Pt/CdS.

2. The photo of CdS, 1%Pt/CdS and 2%Pt/CdS

Supplementary Fig. 2 The photo of photocatalysts. The images showing the real products of CdS, 1%Pt/CdS and 2%Pt/CdS.

3. TEM images showing micro-morphology of CdS, 1%Pt/CdS and 2%Pt/CdS

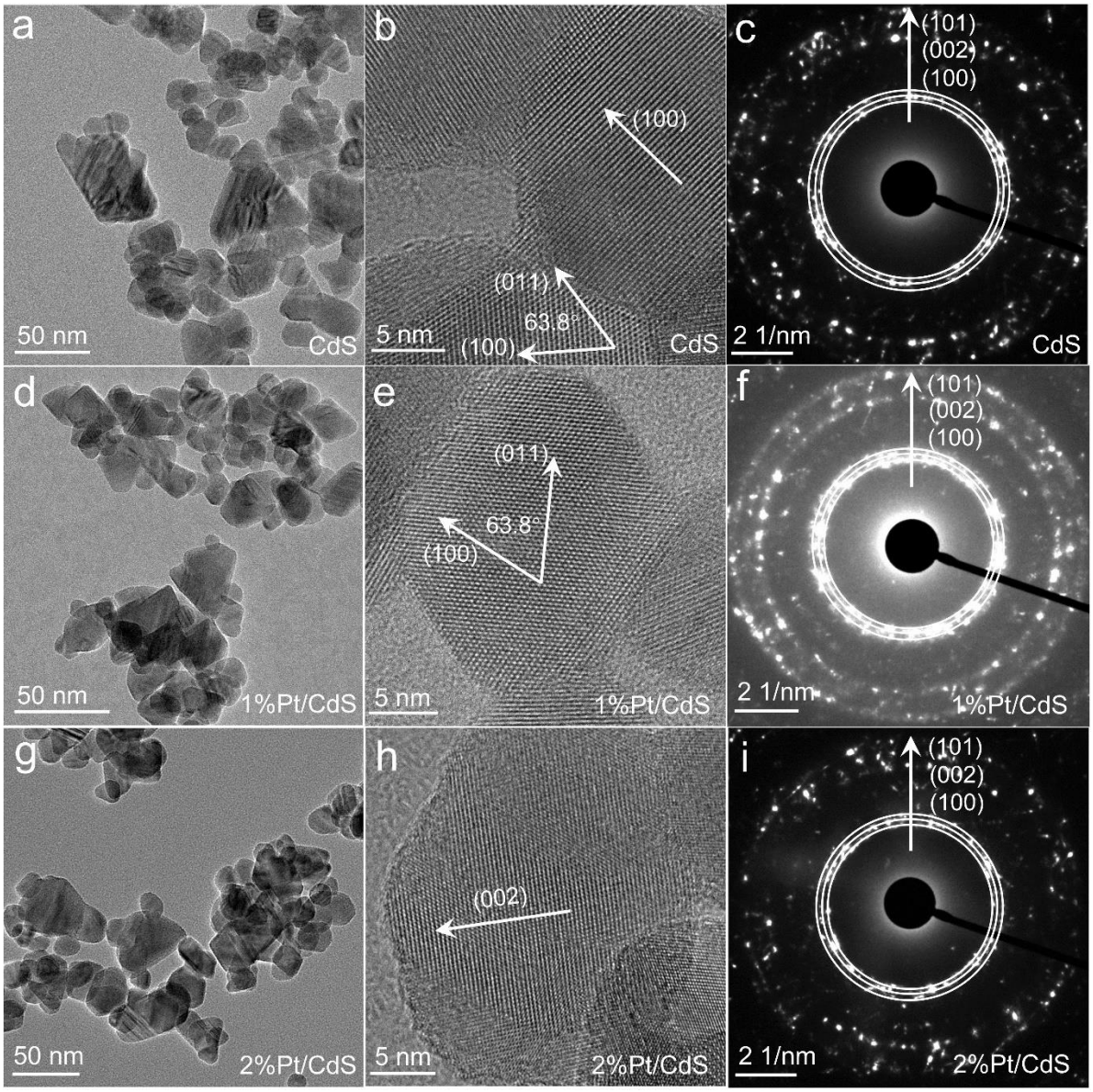

Supplementary Fig. 3 Micro-morphology of photocatalysts. TEM, high-resolution TEM and selected area electron diffraction (SAED) images of CdS **a-c**, 1%Pt/CdS **d-f** and 2%Pt/CdS **g-i**.

4. XPS Cd 3*d*, Pt 4*f* and O 1*s* fine spectra of CdS, 1%Pt/CdS and 2%Pt/CdS

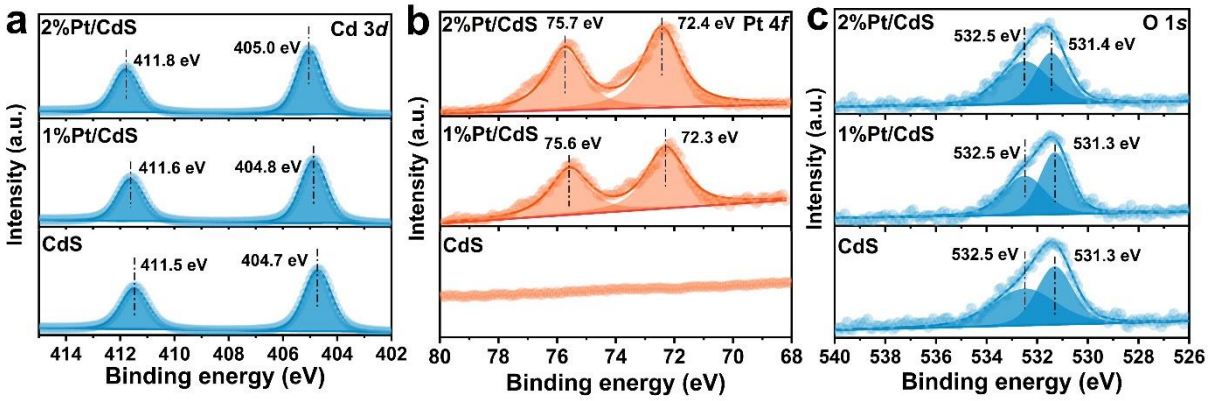

Supplementary Fig. 4 XPS of photocatalysts. X-ray photoelectron Cd 3*d* **a**, Pt 4*f* **b**, O 1*s* **c** fine spectra of CdS, 1%Pt/CdS and 2%Pt/CdS.

5. XPS S 2*p* fine spectra of CdS, 1%Pt/CdS and 2%Pt/CdS

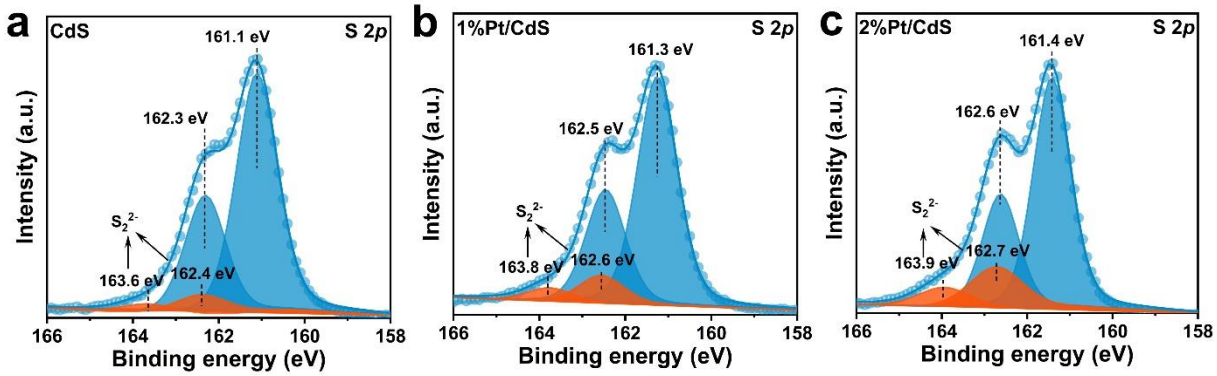

Supplementary Fig. 5 XPS of photocatalysts. X-ray photoelectron S 2*p* fine spectra of CdS **a**, 1%Pt/CdS **b** and 2%Pt/CdS **c**.

6. XPS Cl 2*p* fine spectra and full spectra of CdS, 1%Pt/CdS and 2%Pt/CdS

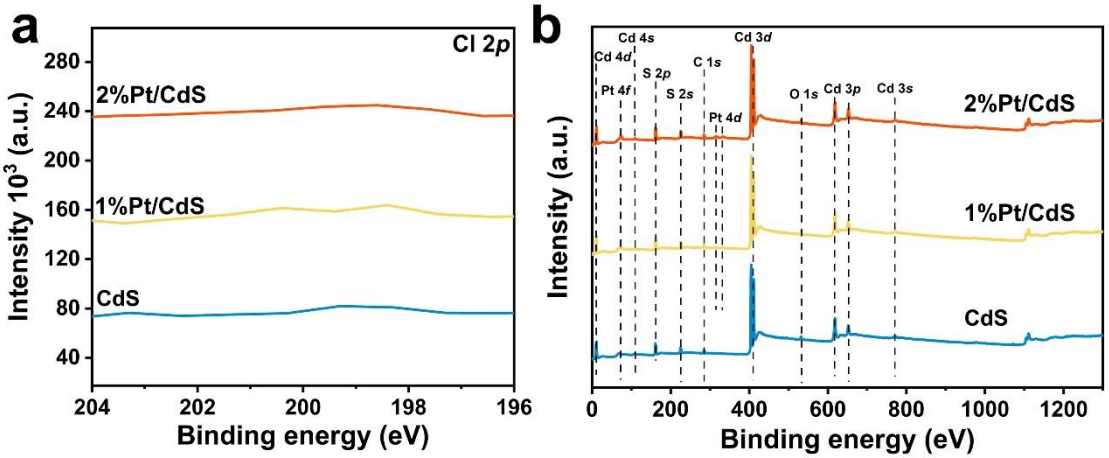

Supplementary Fig. 6 XPS of photocatalysts. X-ray photoelectron Cl 2*p* fine spectra **a** and full spectra **b** of CdS, 1%Pt/CdS and 2%Pt/CdS.

7. EPR for CdS and 1%Pt/CdS

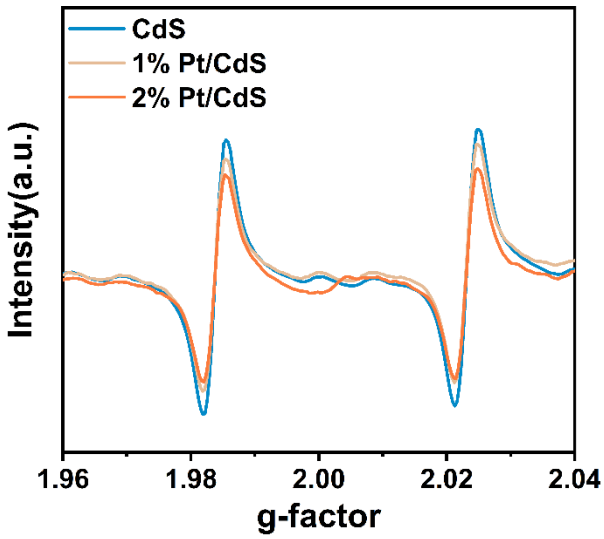

Supplementary Fig. 7 Crystal defects revelation. EPR of CdS, 1%Pt/CdS and 2%Pt/CdS.

The EPR signals over CdS were ascribed to the crystal defects induced by unsaturated sulfur. The loading of Pt decreased the distribution of defects, indicating Pt was anchored on unsaturated sulfur sites.

8. k^3-weighted EXAFS of Pt foil, PtO_2, 1%Pt/CdS and 2%Pt/CdS

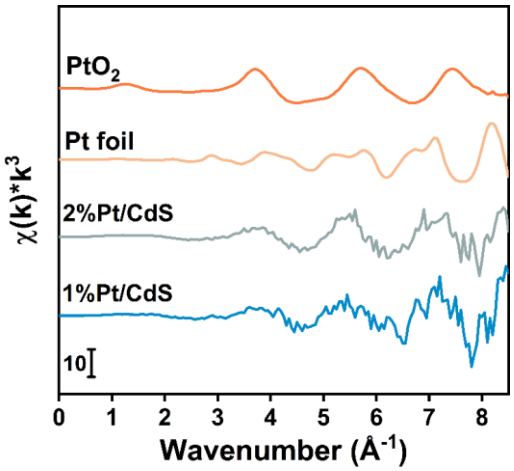

Supplementary Fig. 8 Coordination revelation. k^3-weighted extended X-ray absorption fine structure of 1%Pt/CdS, 2%Pt/CdS, Pt foil and PtO_2.

9. CO adsorption and desorption in-situ DRIFTS

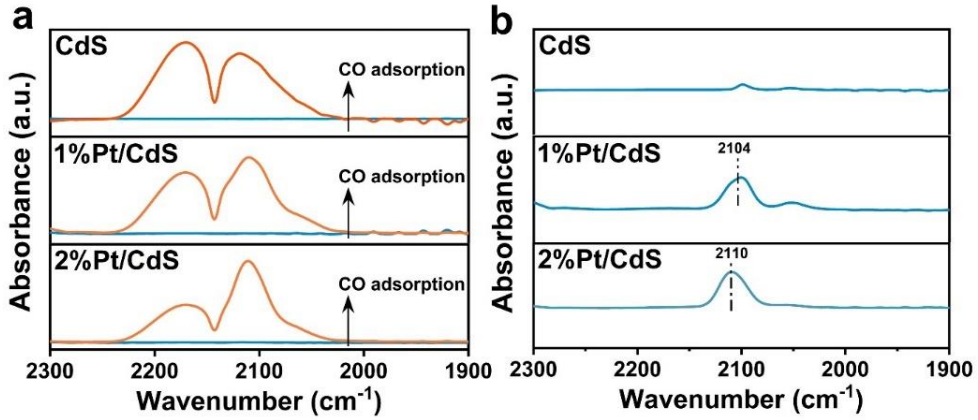

Supplementary Fig. 9 CO adsorption and desorption in-situ DRIFTS. CO adsorption **a** and CO desorption **b** in-situ DRIFTS of CdS, 1%Pt/CdS and 2%Pt/CdS (The data were smoothed during processing).

10. HAADF-STEM of 1%Pt/CdS and 2%Pt/CdS

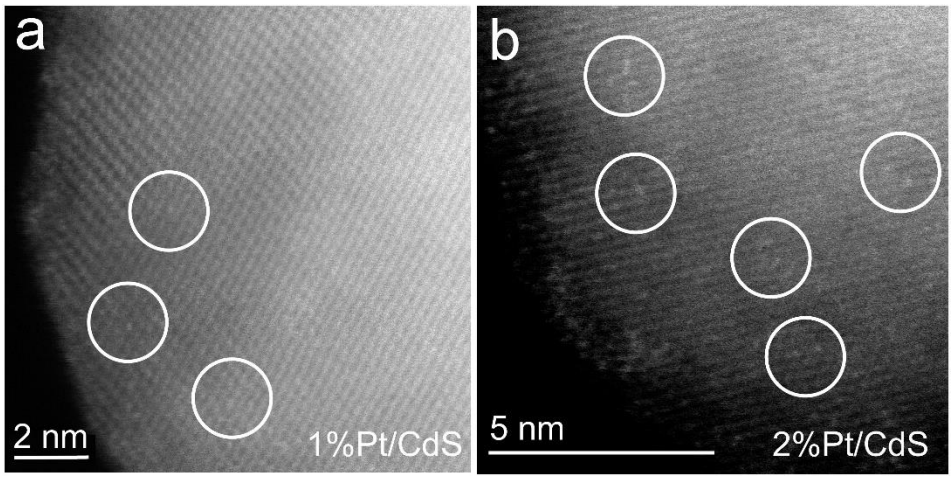

Supplementary Fig. 10 The highly dispersed Pt atom revelation. HAADF-STEM of 1%Pt/CdS **a** and 2%Pt/CdS **b**.

11. The proposed Pt-S configurations over 1%Pt/CdS and 2%Pt/CdS

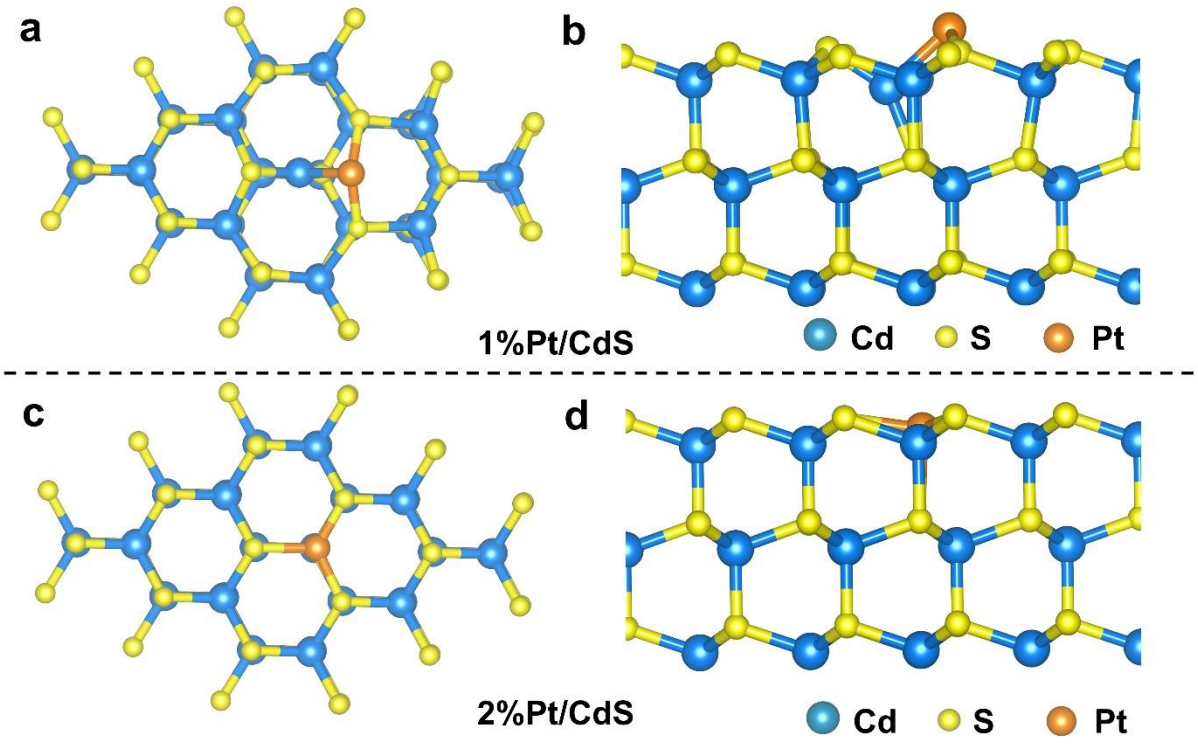

Supplementary Fig. 11 The proposed Pt-S configurations. The top view **a** and side view **b** of proposed 1%Pt/CdS. The top view **c** and side view **d** of proposed 2%Pt/CdS.

12. Steady-state absorption of CdS, Pt_1/CdS and Pt_2/CdS

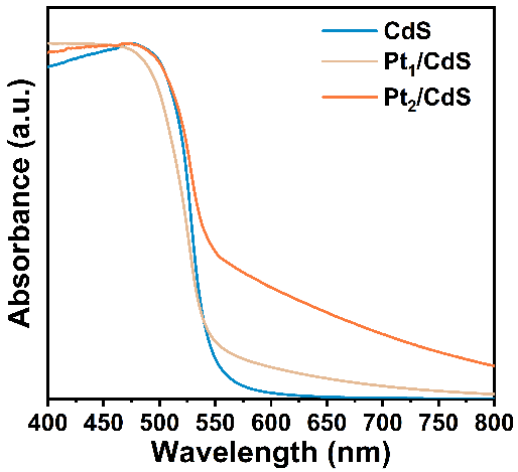

Supplementary Fig. 12 Steady-state absorption of photocatalysts. Ultraviolet-visible diffuse and reflectance (UV-vis DRS) spectra of CdS, Pt_1/CdS and Pt_2/CdS.

The dominating absorption peak at ~ 500 nm corresponds to the band edge electron transition in CdS.

13. The band edge position of CdS, Pt_1/CdS and Pt_2/CdS

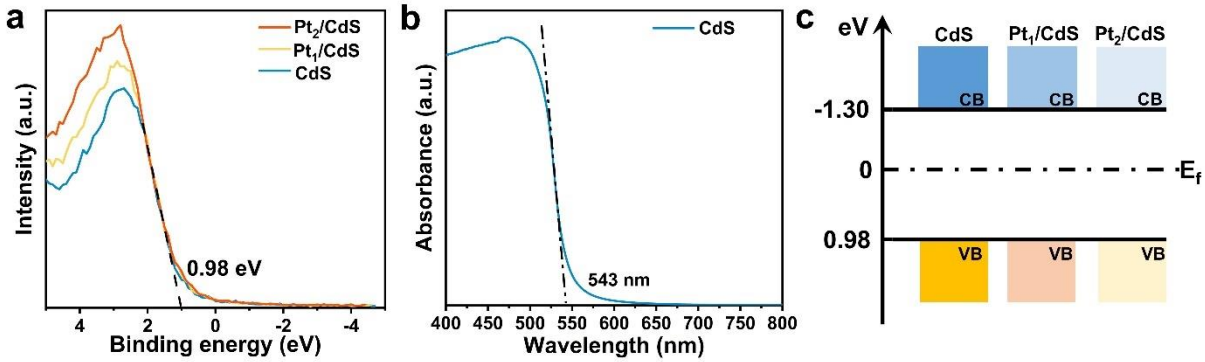

Supplementary Fig. 13 The band edge position of photocatalysts. XPS valence band spectra of CdS, Pt_1/CdS and Pt_2/CdS **a**; the steady-state absorption edge of CdS **b**; the band structure of CdS, Pt_1/CdS and Pt_2/CdS **c**.

14. The kinetic decay curves of CdS with different pump laser pulse fluency

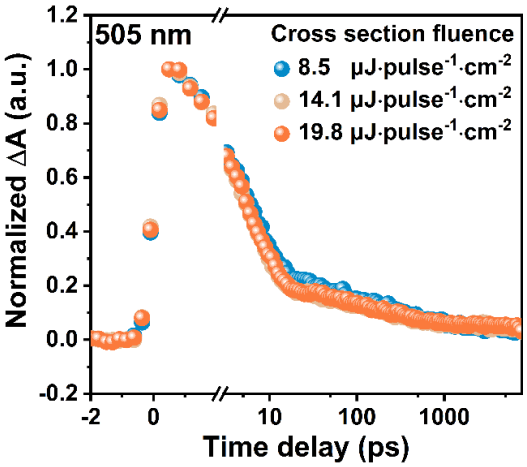

Supplementary Fig. 14 The kinetic decay curves. The ground-state bleach signal decay curves of CdS with different pump light power.

Supplementary Fig. 14 displays the ground state bleach decay of CdS with different pump laser fluence. As previous work indicated (J. Am. Chem. Soc. 143, 20264-20273 (2021)), for multiple exciton dynamics, the decay curve can be strongly influenced by pump laser fluence due to the possible Auger recombination. But in this work, when the cross section fluence is lower than 19.8 $\mu J \cdot pulse^{-1} \cdot cm^{-2}$ (the frequency of excitation is 1000 Hz and the beam diameter is 1.5 mm), the obtained decay curve is almost identical, illustrating there is only single exciton dynamics.

15. Transient absorption spectra of CdS, Pt_1/CdS and Pt_2/CdS

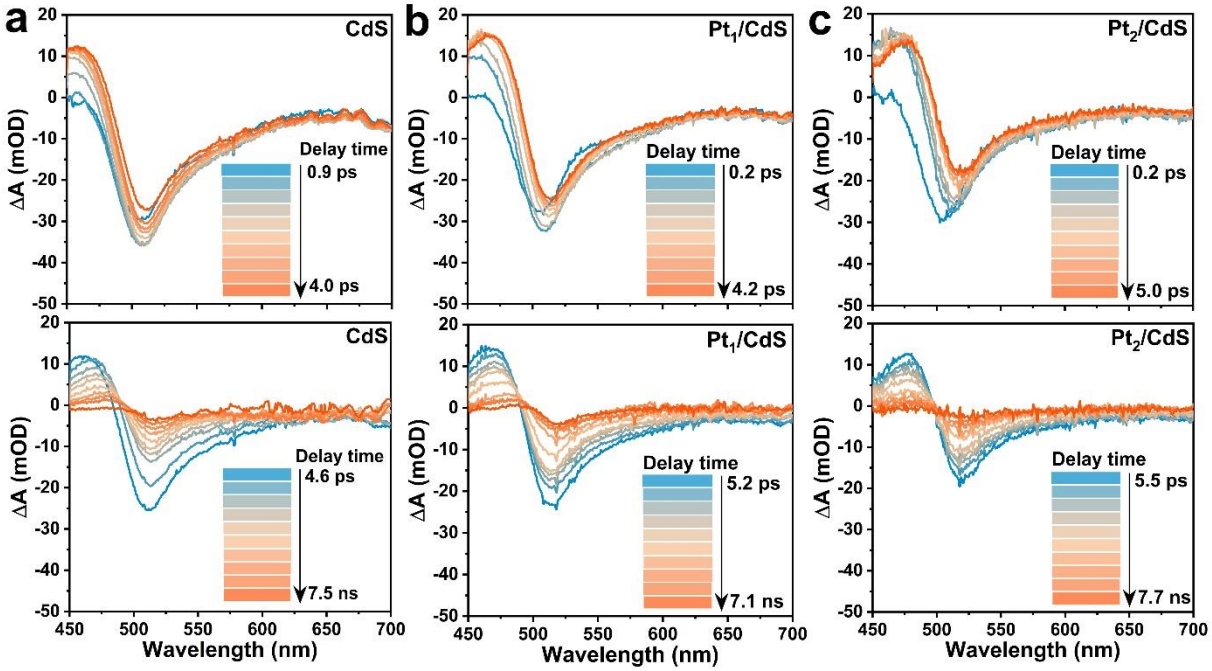

Supplementary Fig. 15 Excited-state dynamics studying. Transient absorption spectra observation of CdS **a**, Pt_1/CdS **b** and Pt_2/CdS **c**, of which time scale ranges from femtosecond to nanosecond.

16. The kinetic decay curves at 600 nm when BQ serves as trapping agents

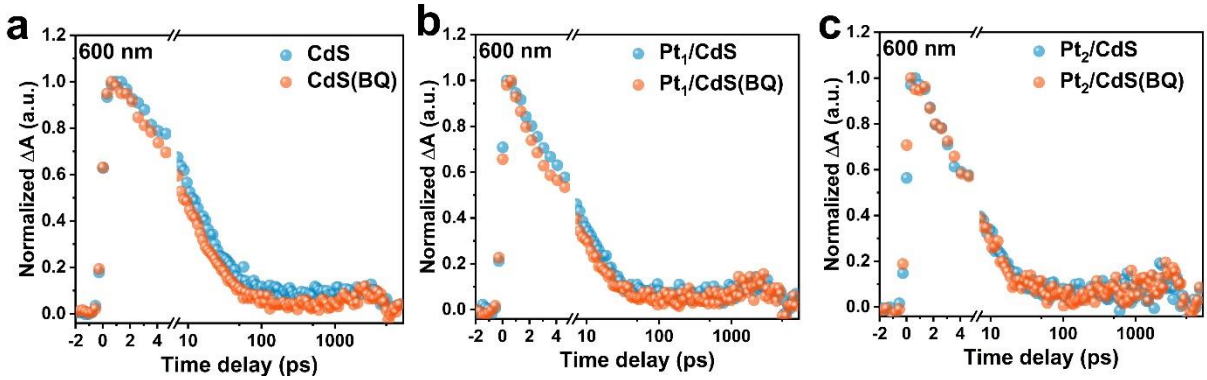

Supplementary Fig. 16 Excited-state dynamics studying. The kinetic decay curves at 600 nm to determine the contribution of p-benzoquinone (BQ) to excited-state carrier relaxation: CdS **a**, Pt_1/CdS **b**, Pt_2/CdS **c**.

17. The kinetic decay curves at 505 nm when BQ serves as trapping agents

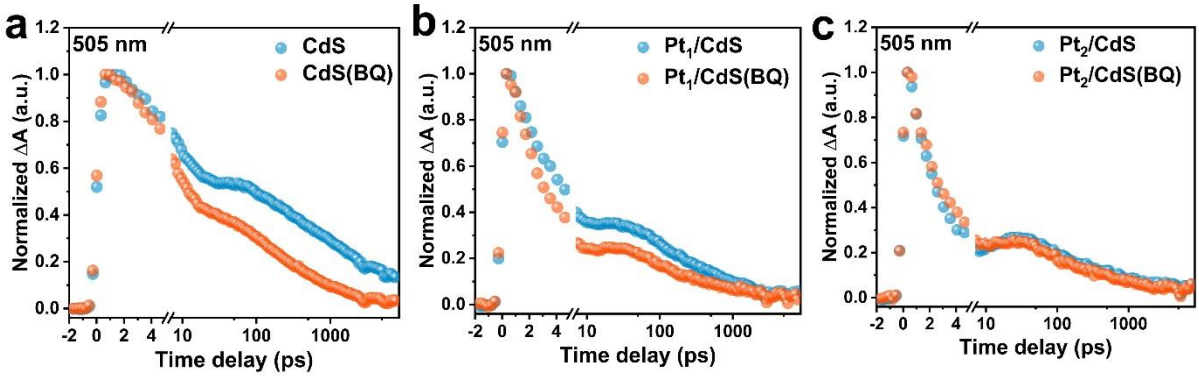

Supplementary Fig. 17 Excited-state dynamics studying. The kinetic decay curves at 505 nm to determine the contribution of p-benzoquinone (BQ) to excited-state carrier relaxation: CdS **a**, Pt_1/CdS **b**, Pt_2/CdS **c**.

18. The steady-state photoluminescence spectra of CdS, Pt_1/CdS and Pt_2/CdS

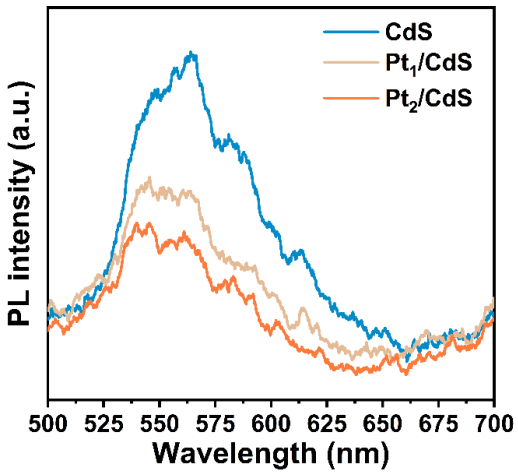

Supplementary Fig. 18 Radiative recombination of photocatalysts. Steady-state photoluminescence (PL) spectra of CdS, Pt_1/CdS and Pt_2/CdS (excitation photon wavelength: 360 nm).

19. In-situ XPS Cd 3*d* fine spectra of CdS, Pt_1/CdS and Pt_2/CdS

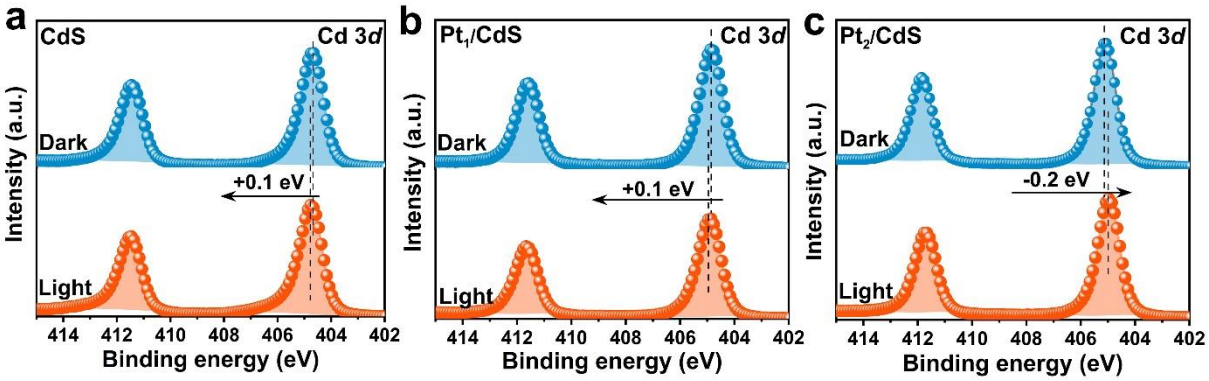

Supplementary Fig. 19 In-situ XPS spectra of photocatalysts. Cd 3*d* fine spectra in dark and light field: CdS **a**, Pt_1/CdS **b**, Pt_2/CdS **c**.

20. Transient photocurrent response of CdS, Pt_1/CdS and Pt_2/CdS

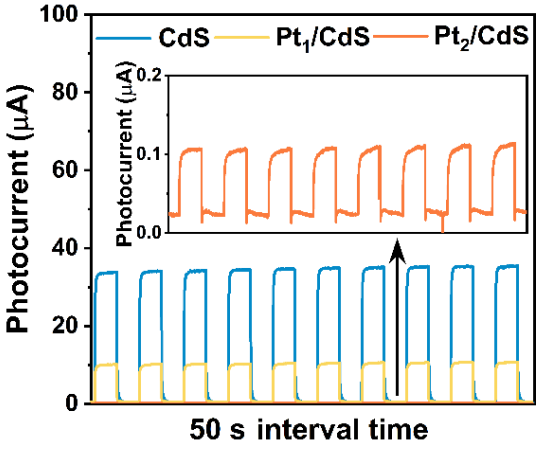

Supplementary Fig. 20 Photoelectrochemical evaluations. Transient photocurrent response of CdS, Pt_1/CdS and Pt_2/CdS (embedding picture shows the enlarged Pt_2/CdS photocurrent image and the applied voltage is not iR corrected).

21. Incident monochromatic photon-electron conversion efficiency (IPCE) measurement

The IPCE of samples was measured in the wavelength range of 450-700 nm based on Equation (1) (Adv. Energy Mater. 11, 2003233 (2025)), where I_{ph} represents the photocurrent intensity at a specific wavelength, λ represents the wavelength of photons, and P_{mono} is the power of monochromatic light. Supplementary Table 6 summarizes the parameters of IPCE calculation. IPCE measurements are only performed once.

$$IPCE = \frac{1240(V \times nm) \times |I_{ph}(mA)|}{P_{mono}(mW) \times \lambda(nm)} \quad (1)$$

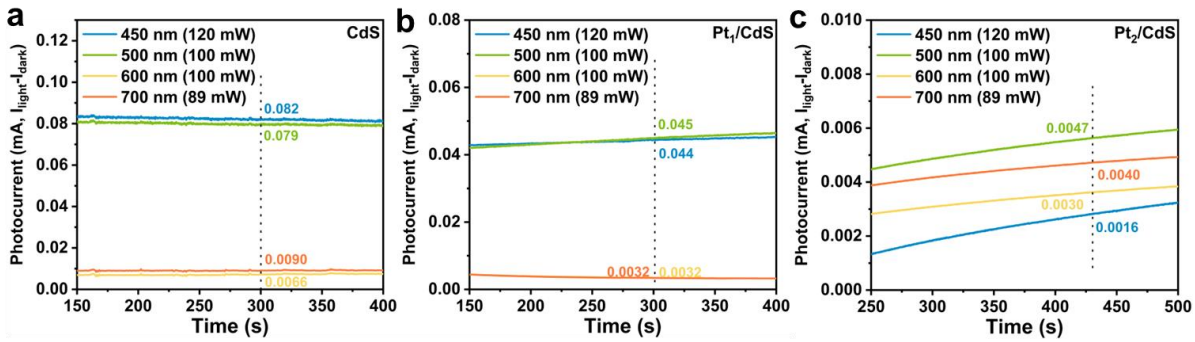

Supplementary Fig. 21 IPCE measurements. The photon-induced current in the circuit where the working electrode made of CdS film **a,** Pt_1/CdS film **b** and Pt_2/CdS film **c** (The applied voltage is not iR corrected).

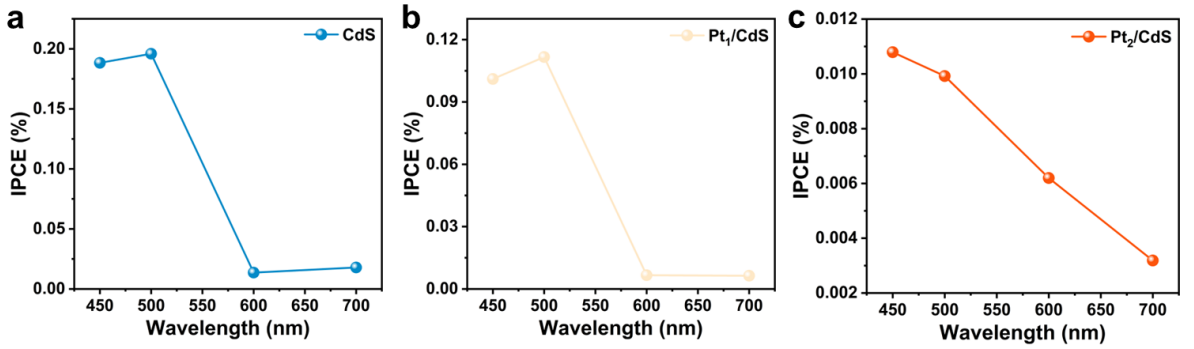

Supplementary Fig. 22 IPCE measurements. IPCE of CdS **a**, Pt_1/CdS **b** and Pt_2/CdS **c** (The applied voltage is not iR corrected).

22. Contrast experiments to determine the optimized photocatalyst amount

Supplementary Fig. 23 The photo of photocatalytic reactor. The photo of glass reactors for photocatalytic CH_4 conversion evaluation.

23. Photocatalytic evaluation on Pt_x/CdS (X=0.5 to 2)

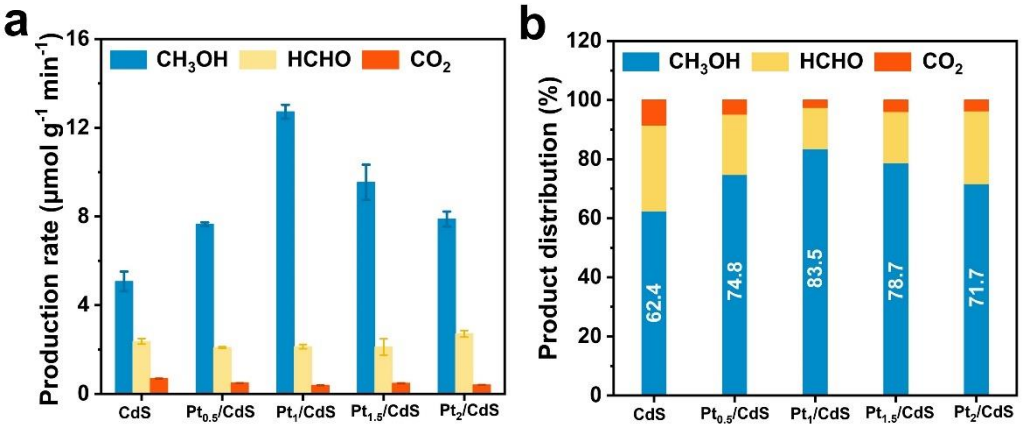

Supplementary Fig. 24 Photocatalytic CH_4 oxidation performance evaluation. a The contribution of Pt amount to the statistic average products production rate and **b** products distributions. Error bar represents standard deviations obtained from at least three independent measurements.

24. Photocatalytic cycle experiments results

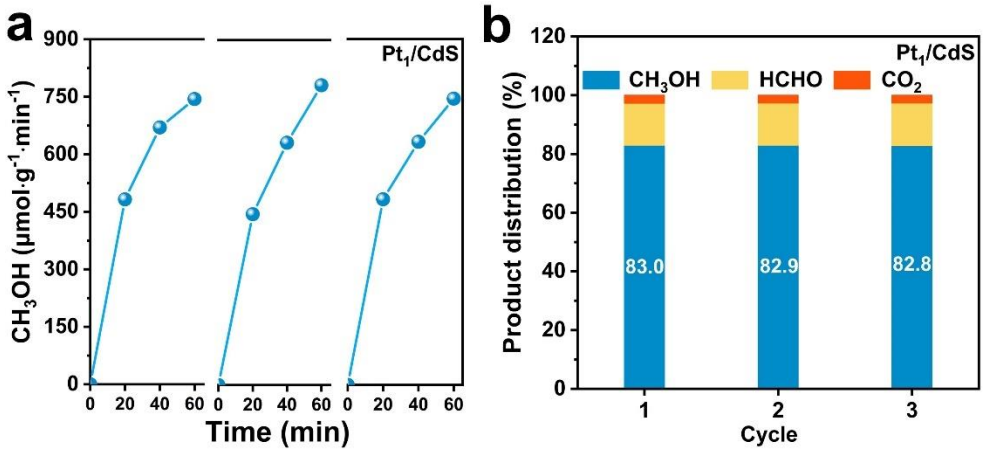

Supplementary Fig. 25 Photocatalytic CH_4 to CH_3OH cycle experiments over Pt_1/CdS. **a** The linear graph showing the CH_3OH amount in the system. **b** The average product distribution in every cycle.

25. XRD of used photocatalyst

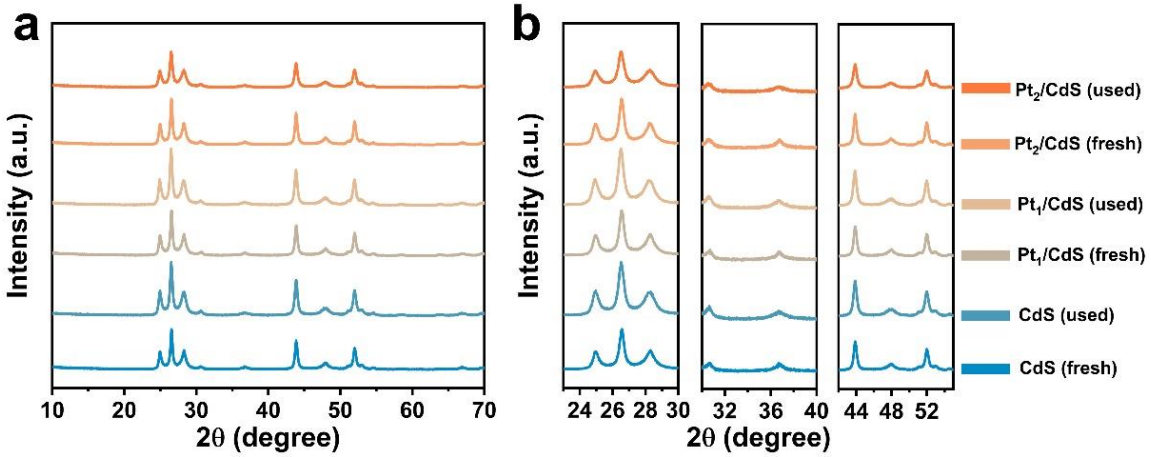

Supplementary Fig. 26 XRD of fresh and used photocatalysts: **a** full spectra and **b** partially enlarged spectra of XRD.

26. XPS Cd 3*d*, S 2*p* and O 1*s* fine spectra of used photocatalyst

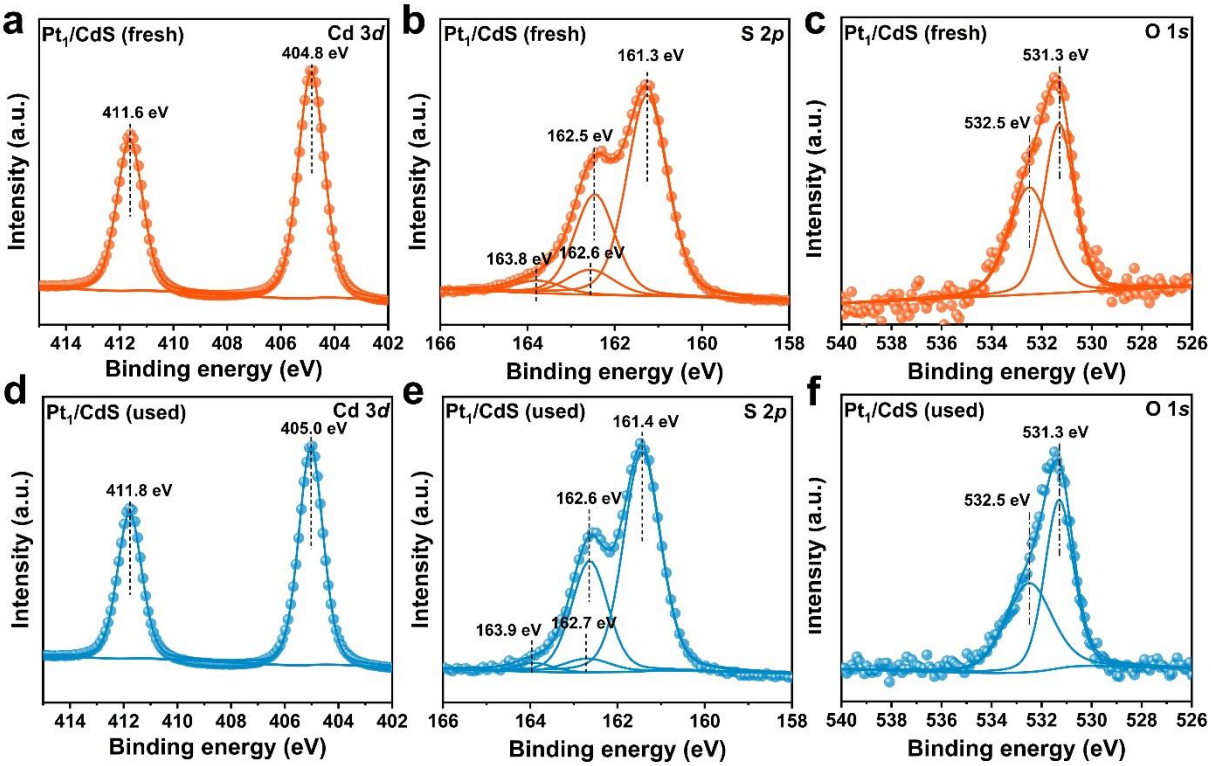

Supplementary Fig. 27 XPS of fresh and used photocatalyst. XPS Cd 3*d*, S 2*p* and O 1*s* fine spectra of fresh Pt_1/CdS **a-c** and used Pt_1/CdS **d-f**.

27. XPS S 2*p* and Pt 4*f* fine spectra of used photocatalyst

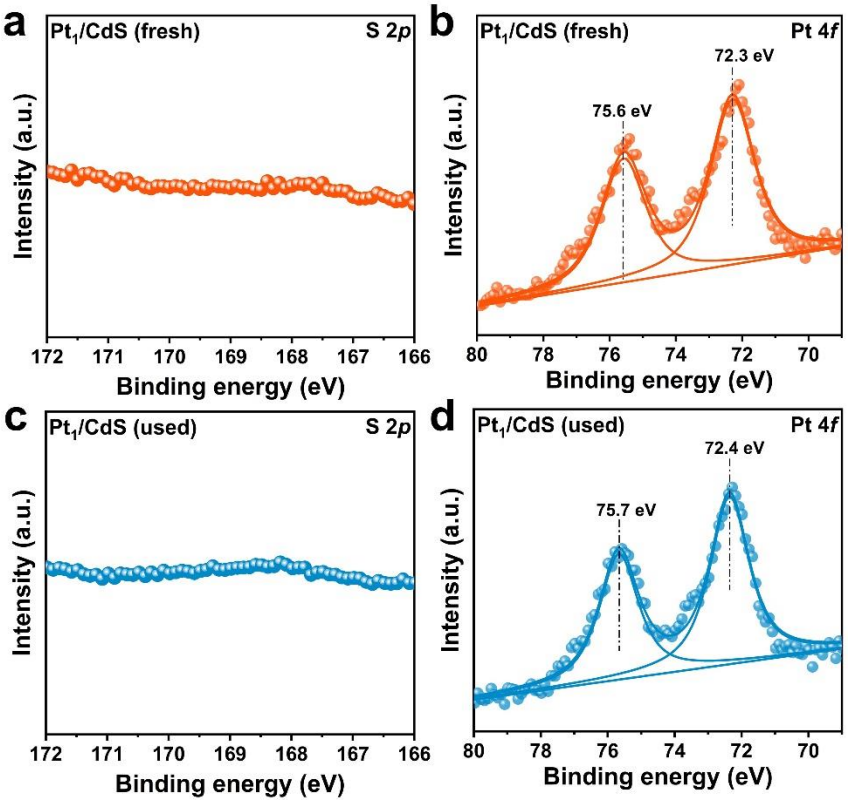

Supplementary Fig. 28 XPS of fresh and used photocatalyst. XPS S 2*p* and Pt 4*f* fine spectra of fresh Pt_1/CdS **a-b** and used Pt_1/CdS **c-d**.

28. The performance comparison for Pt_1/CdS and Pt_2/CdS

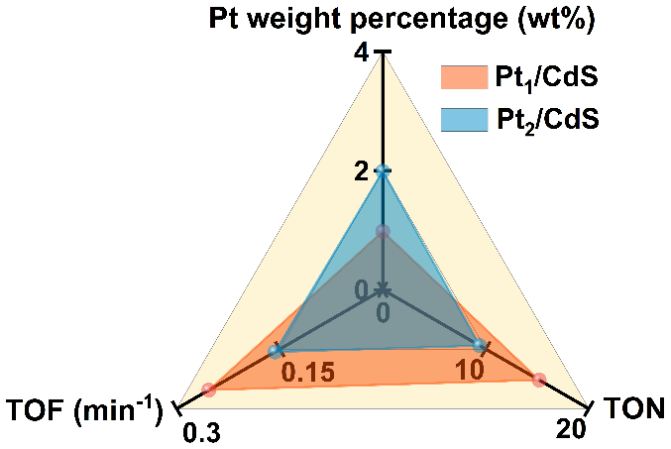

Supplementary Fig. 29 The performance comparison for Pt_1/CdS and Pt_2/CdS. TON and TOF over Pt_1/CdS and Pt_2/CdS.

CH_3OH production amount over Pt_1/CdS is 763.4 ± 19.7 μmol g^{-1} in 1 h, and photocatalyst amount is 10 mg. Considering that Pt weight percentage in Pt_1/CdS is ~0.98 wt%, the amount of Pt participating in photocatalytic CH_4 conversion is 0.098 mg (0.502 μmol). TON of Pt_1/CdS is determined to be 15.19 ± 0.40 and TOF is 0.25 ± 0.0065 min^{-1}. Same procedures also adapted to Pt_2/CdS.

29. Apparent quantum efficiency (AQE) determination

Supplementary Fig. 30 displays the set-up for apparent quantum efficiency (AQE) determination. The number of incident photon was firstly determined based on Equation S2. Noting that irradiation intensity on irradiation area was attenuated from centra area to the edge (Supplementary Fig. 31a), the specific power of light (*P*) on irradiation area was calculated through double integral. Displayed in Supplementary Fig. 31b**,** the relation of 395 nm irradiation intensity and the distance to central area was revealed using linear fitting, which was further transformed to deduce integral formula (Equation S4). The power of 395 nm moonlight was determined to be 292.3 mW. Furthermore, based on the CH_3OH amount (11.6 ± 0.2 μmol) in 1 h (3600 s), the number of excited electrons was equal to 2.10×10^{19} ($1.16 \times 10^{-5} \times 6.023 \times 10^{23} \times 3$). AQE at 395 nm was finally determined to be 1.00 ± 0.017%. Supplementary Table 8 summarizes the parameters of CH_3OH production AQE calculation.

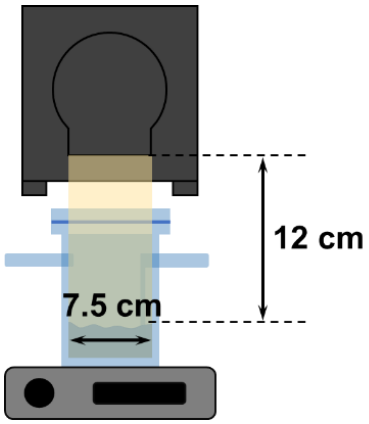

Supplementary Fig. 30 The schematic illustrations (created using Microsoft Powerpoint software) on photocatalytic evaluations. The set-up and the parameters.

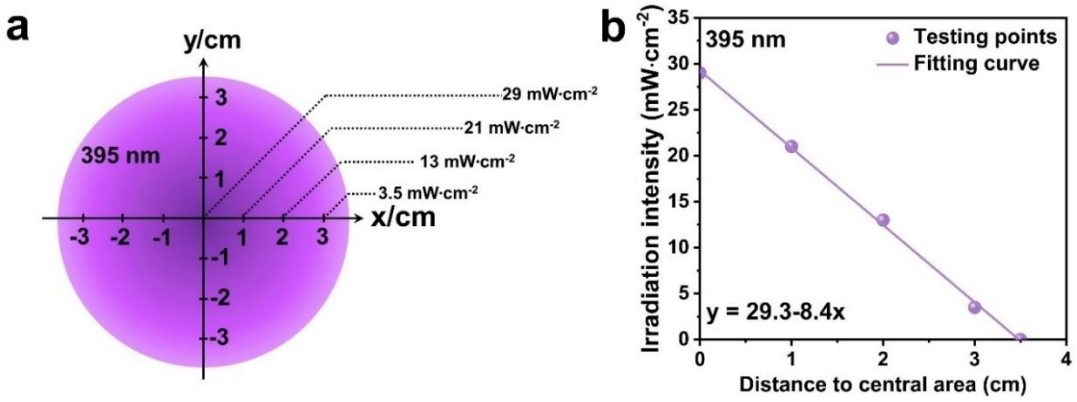

Supplementary Fig. 31 AQE determination. a The diagram illustrating the 395 nm monochromatic light irradiation intensity fluctuation in irradiation area. **b** The fitting curve of irradiation attenuation in irradiation area.

272 $$Number\ of\ incident\ photon = \frac{P \times t \times \lambda}{h \times c} \quad (2)$$

273 $$AQE = \frac{Number\ of\ electron}{Number\ of\ incident\ photon} \quad (3)$$

274 $$P_{395\,nm} = \int_{-3.75}^{3.75} dy \int_{-3.75}^{3.75} 29.3 - 8.4\sqrt{x^2 + y^2}\, dx \quad (4)$$

275

30. In-situ DRIFTS in the atmosphere of CH_4+H_2O+O_2

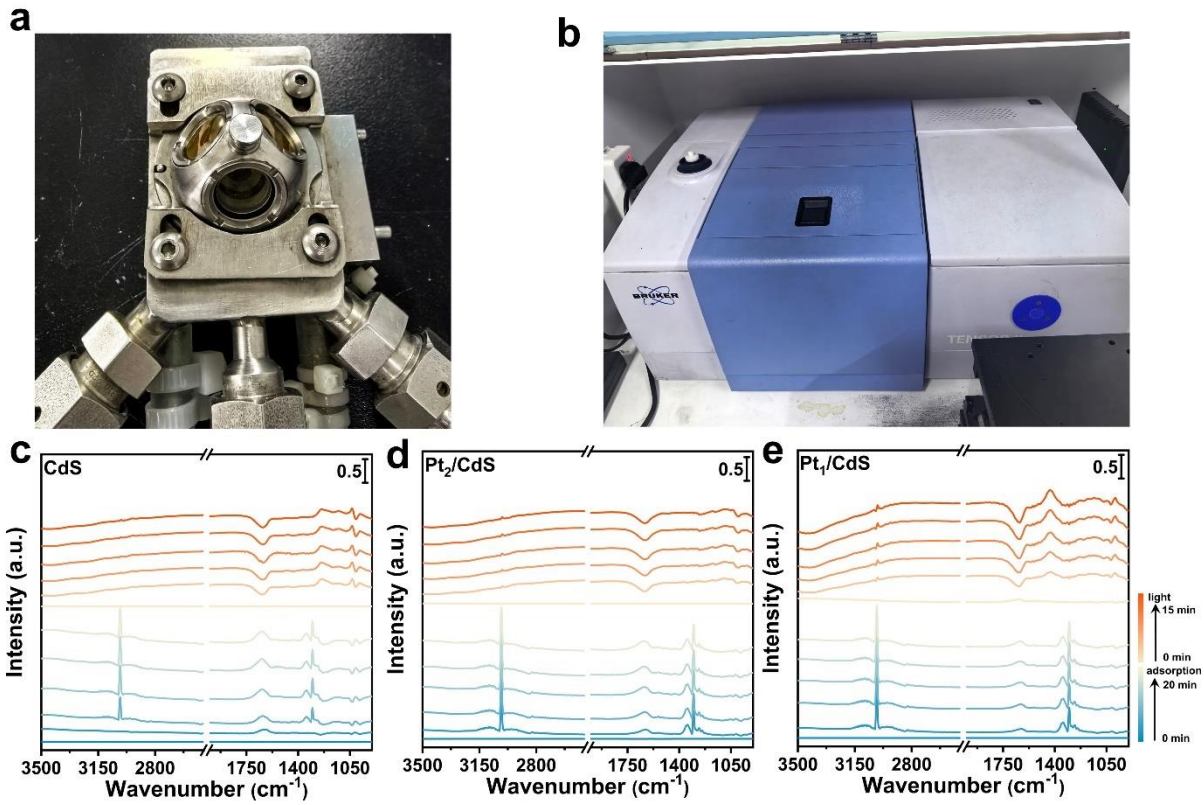

Supplementary Fig. 32 Reaction mechanism revelation. a The Harrick Praying Mantis three-window diffuse-reflectance cell and **b** Bruker infrared spectrometer (Tensor II) equipped with a liquid-nitrogen-cooled mercury-cadmium-telluride (MCT) detector for in-situ DRIFTS. In-situ DRIFTS of CdS **c**, Pt_2/CdS **d** and Pt_1/CdS **e** in the atmosphere of CH_4 + O_2 + H_2O under light irradiation. The sample surface has been fully adsorbed with reactants before the light irradiation and these data were smoothed during processing.

31. In-situ DRIFTS in the atmosphere of CH_4+H_2O

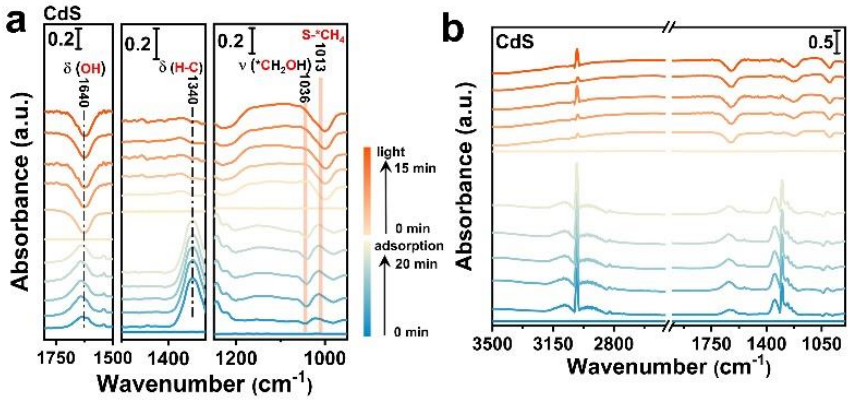

Supplementary Fig. 33 In-situ diffuse reflectance infrared Fourier transform spectroscopy (DRIFTS) of CdS in the atmosphere of CH_4 + H_2O under light irradiation. a the partially-enlarged spectra **a** and **b** full spectra. The sample surface has been fully absorbed with reactants before the light irradiation and these data were smoothed during processing.

In the atmosphere of CH_4 and H_2O, a prominent signal at 1013 cm^{-1} was still found over CdS in the adsorption process, which could be ascribed to S-*CH_4 configuration. Under the light irradiation, S-*CH_4 signal decreased due to the dissociation of configuration. Simultaneously, as O_2 was absent in the atmosphere, oxygen-containing groups amount is remarkably decreased but *CH_2OH can still be detected.

32. In-situ EPR spectra under different testing conditions

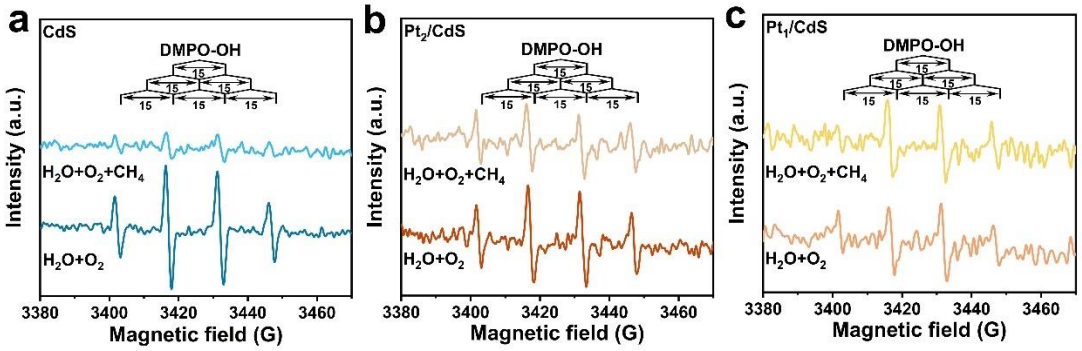

Supplementary Fig. 34 Radicals distributions revelation. In-situ electron paramagnetic resonance (EPR) spectroscopy of CdS **a**, Pt_2/CdS **b** and Pt_1/CdS **c** under different testing conditions. (These data were smoothed during processing)

For CdS and Pt_2/CdS, it should be noted that when CH_4 is further bubbled into aerobic water ($H_2O+O_2+CH_4$), the intensity of detected ·OH is obviously declined, indicating that CH_4 adsorption and ·OH generation are carried out on same sites. As to Pt_1/CdS, ·OH amount is not declined with the introduction of CH_4, demonstrating the separated sites for CH_4 adsorption/activation and ·OH generation.

33. In-situ EPR spectra in aerobic CH_3OH

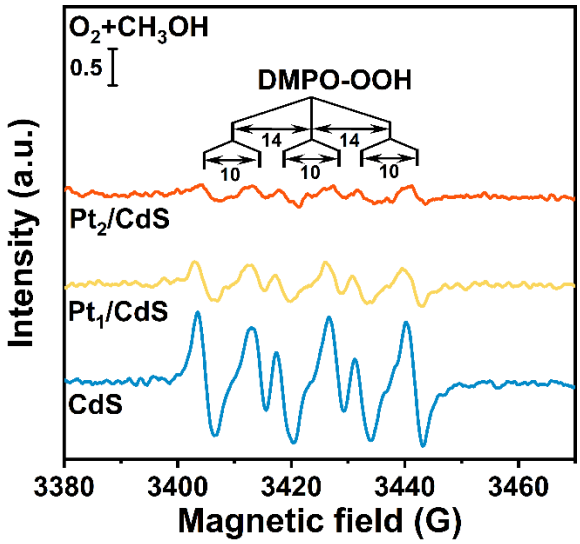

Supplementary Fig. 35 Radicals distributions revelation. In-situ electron paramagnetic resonance (EPR) spectroscopy of CdS, Pt_1/CdS and Pt_2/CdS. (These data were smoothed during processing)

Methanol (CH_3OH) can remove ·OH and exaggerate ·OOH signal. The intensified ·OOH was found over CdS in contrast to Pt_1/CdS and Pt_2/CdS, because ·OOH can hardly be reduced with scarce electron-rich sites. As to Pt_2/CdS, the abundant Pt sites greatly promote electron-injection behavior, and O_2 can be fully reduced to ·OH with limited intermediates ·OOH detected.

34. N_2 adsorption-desorption isotherms curves

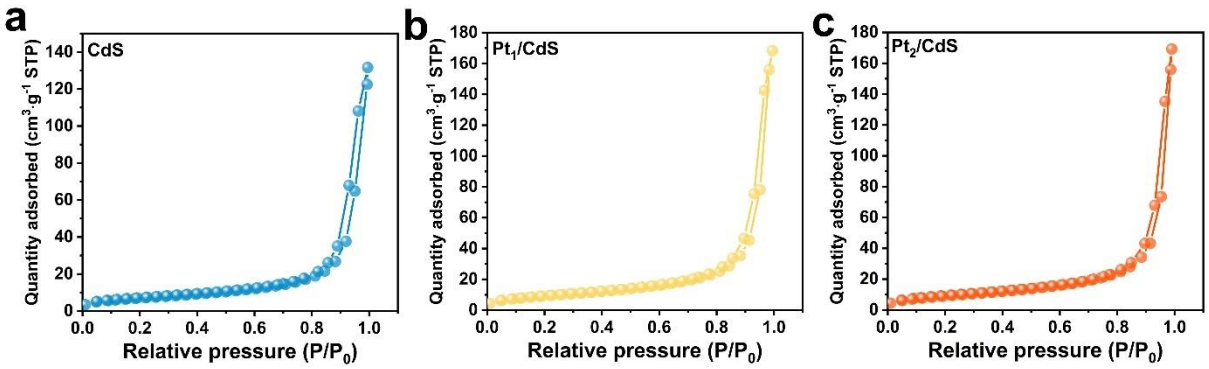

Supplementary Fig. 36 The specific surface of photocatalysts. N_2 adsorption-desorption isotherms of CdS **a**, Pt_1/CdS **b** and Pt_2/CdS **c**.

Supplementary Tables

1. The crystal average thickness of CdS, 1%Pt/CdS and 2%Pt/CdS

Supplementary Table 1 The average thickness on crystal facet direction of CdS, 1%Pt/CdS and 2%Pt/CdS.

Crystal facet	CdS (nm)	1%Pt/CdS (nm)	2%Pt/CdS (nm)
(100)	20.21	25.86	27.17
(002)	32.27	30.68	31.27
(101)	15.97	17.05	18.83
(102)	17.34	12.42	21.38
(110)	27.40	25.35	27.05
(103)	15.57	15.21	17.83
(200)	30.12	28.08	30.54
(112)	33.47	31.77	29.12
(201)	17.84	17.95	20.27

The average thickness on crystal facet direction is calculated by the Scherrer Formula:

$$D = \frac{K\lambda}{B\cos\theta} \quad (5)$$

K represents the Scherrer constant and it was equal to 0.89. λ was the wavelength of X-ray (1.54056 Å) and *B* was the full width at half maximum (FWHM) of diffraction peaks, which was obtained through Jade software. Moreover, θ is the diffraction angle of representative crystal facets.

2. The EXAFS fitting parameters for 1%Pt/CdS

Supplementary Table 2 Curve-fit parameters of Pt L_3-edge EXAFS of 1%Pt/CdS based on optimized crystal model.

	S_0^2	δ^2	ΔE_0 (eV)	R (Å)	N	*R-factor*
Pt-S[1]	0.98	0.0012 ± 0.0032	7.17 ± 2.87	2.33	2.58 ± 0.82	0.017
Pt-Cd[2]		-0.0018 ± 0.0097		2.79	1.00 ± 1.71	

S_0^2 was set as 0.98; σ^2: Debye-Waller factors; ΔE^0: the inner potential correction; R: bond distance; N: coordination numbers; *R factor*: goodness of fit.

3. The EXAFS fitting parameters for 2%Pt/CdS

Supplementary Table 3 Curve-fit parameters of Pt L_3-edge EXAFS of 2%Pt/CdS based on optimized crystal model.

	S_0^2	δ^2	E_0 (eV)	R (Å)	N	*R-factor*
Pt-S¹	0.98	-0.00013 ± 0.0086	5.98 ± 4.0028	2.28	2.75 ± 1.87	0.019
Pt-S²		-0.0060 ± 0.0055		2.42	1.10 ± 0.01	

S_0^2 was set as 0.98; σ^2: Debye-Waller factors; ΔE^0: the inner potential correction; R: bond distance; N: coordination numbers; *R factor*: goodness of fit.

4. The TAS fitting parameters

Supplementary Table 4 Time-components parameters derived from transient adsorption spectra (TAS) kinetic fitting.

Samples	Time-components				
CdS	τ_0	τ_{et}	τ_1	τ_2	Inf
	3.5 ps	-	13.4 ps	397.0 ps	>8 ns
Pt_1/CdS	τ_0	τ_{et}	τ_1	τ_2	Inf
	0.81 ps	3.3 ps	10.6 ps	344.8 ps	>8 ns
Pt_2/CdS	τ_0	τ_{et}	τ_1	τ_2	Inf
	0.80 ps	1.6 ps	5.4 ps	137.3 ps	>8 ns

5. The TRPL fitting parameters

Supplementary Table 5 Photoluminescence time-components parameters derived from TRPL kinetic fitting.

Samples	PL time-components			
	τ_1 (ns) / A_1(%)	τ_2 (ns) / A_2(%)	τ_3 (ns) / A_3(%)	τ_{avg} (ns)
CdS	2.1 / 72.6	15.4 / 24.2	368.6 / 3.2	258.6
Pt_1/CdS	1.9 / 73.8	12.0 / 24.0	138.9 / 2.2	62.9
Pt_2/CdS	1.9 / 73.3	22.2 / 24.3	121.4 / 2.4	49.1

6. Parameters for Incident monochromatic photon-electron conversion efficiency (IPCE) determination

Supplementary Table 6 The parameters for IPCE determination.

Samples	Wavelength (nm)	Photocurrent (mA)	Power of light (mW)	IPCE (%)
CdS	450	0.082	120	0.19
	500	0.079	100	0.20
	600	0.0066	100	0.014
	700	0.009	89	0.018
Pt_1/CdS	450	0.044	120	0.10
	500	0.045	100	0.11
	600	0.0032	100	0.0066
	700	0.0032	89	0.0064
Pt_2/CdS	450	0.0047	120	0.011
	500	0.004	100	0.0099
	600	0.003	100	0.0062
	700	0.0016	89	0.0032

7. CH_4 conversion and product generation rate

Supplementary Table 7 CH_4 conversion rate and product generation rate.

Samples	CH_3OH production rate ($\mu mol \cdot g^{-1} \cdot min^{-1}$)	HCHO production rate ($\mu mol \cdot g^{-1} \cdot min^{-1}$)	CO_2 production rate ($\mu mol \cdot g^{-1} \cdot min^{-1}$)	The average selectivity of CH_3OH (%)
CdS	5.07 ± 0.44	2.37 ± 0.12	0.69 ± 0.0099	62.3
$Pt_{0.5}$/CdS	7.65 ± 0.089	2.09 ± 0.036	0.49 ± 0.0066	74.8
Pt_1/CdS	12.72 ± 0.31	2.13 ± 0.095	0.39 ± 0.010	83.5
$Pt_{1.5}$/CdS	9.54 ± 0.79	2.11 ± 0.37	0.48 ± 0.016	78.7
Pt_2/CdS	7.88 ± 0.34	2.71 ± 0.15	0.41 ± 0.0090	71.7

8. Parameters for apparent quantum efficiency (AQE) determination

Supplementary Table 8 The parameters for CH_3OH production AQE determination.

Wavelength (λ, nm)	Power of light (P, mW)	Number of incident photon	Amount of CH_3OH in 1 h (μmol)	Number of electrons	AQE (%)
395	292.3	2.09×10^{21}	11.6 ± 0.2	$(2.10 \pm 0.036)\times10^{19}$	1.00 ± 0.017

9. Calculated CH_4 adsorption energy

Supplementary Table 9 The energy of different configurations which are used to calculate adsorption energy.

Configurations	Energy-AB (eV)	Energy-A (eV)	Energy-B (eV)	Adsorption energy (eV)
Pt_1/CdS (Pt) + CH_4	-159.85	Pt_1/CdS (S) -135.70	CH_4 -24.05	-0.098
Pt_1/CdS (S) + CH_4	-159.95	Pt_1/CdS (Pt) -135.70	CH_4 -24.05	-0.19

10. BET surface area and pore size

Supplementary Table 10 The BET surface area and pore size of CdS Pt_1/CdS and Pt_2/CdS.

	CdS	Pt_1/CdS	Pt_2/CdS
BET surface area (m^2/g)	25.7	34.3	34.6
BET adsorption average pore diameter (nm)	31.7	30.3	30.3
BET desorption average pore diameter (nm)	22.9	20.4	18.5

11. Recent representative studies on the photocatalytic oxidation of CH_4 to CH_3OH.

Supplementary Table 11 Recent representative studies on the photocatalytic oxidation of CH_4 to CH_3OH.

Number	Photocatalyst	Reactants	CH_3OH production rate ($\mu mol \cdot g^{-1} \cdot min^{-1}$)	Light Source	Year	Reference
0	Pt_1/CdS	5 mL CH_4, 10% O_2, 20 mL H_2O	12.7	Xe lamp, 600 $mW \cdot cm^{-2}$	/	This work
1	$Fe/Au\text{-}STO_v$	CH_4 / O_2 = 19:1 (bar), 30 mL H_2O	125.5	Xe lamp, 150 $mW \cdot cm^{-2}$	2025	*J. Am. Chem. Soc.* **147**, 38, 34959-34971 (2025)
2	$AuPd_{0.5}/ZnO$	29 bar CH_4, 1 bar O_2, 30 mL H_2O	135.0	Xe lamp, 300 $mW \cdot cm^{-2}$	2024	ACS Catal. **14**, 955-964 (2024)
3	Au_9Pd_1/ZnO	19 bar CH_4, 1 bar O_2, 75 mL H_2O	1393.3	Xe lamp, 350 $mW \cdot cm^{-2}$	2024	Adv. Energy Mater. **14**, 2303642 (2024).
4	$A\text{-}N\text{-}TiO_2$	4 $mL \cdot min^{-1}$, humidified CH_4/Ar gas	2.7	Xe lamp, 350 $mW \cdot cm^{-2}$	2024	ACS Appl. Mater. Interfaces **16**, 4600-4605 (2024).
5	$2Cu/CeO_2$	1.2 MPa CH_4 (95% in Ar), 1.2 MPa CO_2 (99.999%), 50 mL H_2O	1.5	Xe lamp	2023	ACS Sustainable Chem. Eng. **11**, 5537-5546 (2023).
6	Au_{NPs}/In_2O_3	10 bar O_2, 20 bar CH_4, 180 mL H_2O	33.0	Xe lamp, 250 $mW \cdot cm^{-2}$	2023	J. Am. Chem. Soc. **145**, 2698-2707 (2023).
7	Ga_2O_3	5 mL CH_4, 10 mL H_2O	5.4	Xe lamp, 600 $mW \cdot cm^{-2}$	2023	J. Am. Chem. Soc. **145**, 8609-8620 (2023).
8	BN	5 mL CH_4, 10% O_2, 20 mL H_2O	1.3	Xe lamp, 660 $mW \cdot cm^{-2}$	2023	Angew. Chem. Int. Ed. **62**, e202302196 (2023).
9	ZnO/Fe_2O_3	CH_4, 5 mL H_2O	2.0	Xe lamp, 100 $mW \cdot cm^{-2}$	2022	J. Am. Chem. Soc. **144**, 12357-12366 (2022).
10	$TiO_2(001)\text{-}C_3N_4$	8% CH_4, 4% O_2, 165 μL H_2O_2 in 20 mL H_2O	0.3	Xe lamp	2022	Nat. Commun. **13**, 6677 (2022).
11	$Cu\text{-}W\text{-}TiO_2$	20 bar CH_4, 2 bar O_2, 50 mL H_2O	5.0	Xe lamp, 200 $mW \cdot cm^{-2}$, 200 $mW \cdot cm^{-2}$	2022	ACS Catal. **12**, 9515-9525 (2022).
12	$Pd_x\text{-}def\text{-}In_2O_3$	19 bar CH_4, 1 bar O_2, 50 mL H_2O	10.5	420 nm LED lamp	2022	Nat. Commun. **13**, 2930 (2022).

13	$Au_{0.2}Cu_{0.15}$-ZnO	1 bar O_2, 19 bar CH_4, 100 mL H_2O, 25°C	43.3	Xe lamp, 150 mW·cm^{-2}	2022	J. Am. Chem. Soc. **144**, 740-750 (2022)
14	HSiMo/TiO_2	20 bar O_2, 30 bar CH_4, 20 mL H_2O	1.5	Xe lamp	2021	J. Mater. Chem. A **9**, 1713-1719 (2021).
15	q-$BiVO_4$	10 bar CH_4, 10 bar O_2, 10 mL H_2O	12.8	Hg lamp, 170 mW·cm^{-2}	2021	Nat. Sustain. **4**, 509-515 (2021).
16	0.1 wt% Au/ZnO	2 bar CH_4, 1 bar O_2, 100 mL H_2O	34.3	Xe lamp, 100 mW·cm^{-2}	2019	J. Am. Chem. Soc. **141**, 20507-20515 (2019).
17	FeO_x/TiO_2	70 μmol CH_4 in Ar, 8 μmol H_2O_2 in 10 mL H_2O	5.8	Xe lamp	2018	Nat. Catal. **1**, 889-896 (2018).